

THE HYDROGEN EPOCH OF REIONIZATION ARRAY DISH I: BEAM PATTERN MEASUREMENTS AND SCIENCE IMPLICATIONS

ABRAHAM R. NEBEN¹, AARON EWALL-WICE¹, NIPANJANA PATRA², NITHYANANDAN THYAGARAJAN³, JAMES E. AGUIRRE⁴, ZAKI S. ALI², JUDD BOWMAN³ CARINA CHENG², DAVID R. DEBOER² JACQUELINE N. HEWITT², AARON PARSONS²

¹MIT Kavli Institute, Massachusetts Institute of Technology, Cambridge, MA, 02139 USA

²Dept. of Astronomy, University of California, Berkeley, CA, USA

³Arizona State University, School of Earth and Space Exploration, Tempe, AZ 85287, USA and

⁴Dept. of Physics and Astronomy, University of Pennsylvania, Philadelphia, PA

Draft version December 26, 2015

ABSTRACT

The Hydrogen Epoch of Reionization Array (HERA) is a radio interferometer aiming to detect the power spectrum of 21 cm fluctuations from neutral Hydrogen from the Epoch of Reionization. Drawing on lessons from the Murchison Widefield Array (MWA) and the Precision Array for Probing the Epoch of Reionization (PAPER), HERA is a hexagonal array of large (14 m) dishes with suspended dipole feeds designed to maximize sensitivity while economizing data volume. This is the first of a series of four papers characterizing the frequency and angular response of the HERA dish element with simulations and measurements. In this work we measure the angular response at 137 MHz using the ORBCOMM beam mapping system of Neben et al. (2015). We measure collecting areas of 70–100 m² and estimate power spectrum SNRs of 6–8 with one season of HERA-127 observations, making very conservative foreground assumptions. Lastly we simulate foreground visibilities using numerical beam models and study the foreground distribution in Fourier space as a function of LST, and the uncertainties in these predictions due to beam modeling uncertainties. Future measurements will study the dish beam in the presence of adjacent dishes, quantifying levels of cross-talk and cross-coupling.

Subject headings: instrumentation: interferometers — techniques: interferometric — cosmology: observations — dark ages, reionization, first stars

1. INTRODUCTION

A new generation of low frequency radio telescopes is coming online with the goal of probing redshifted 21 cm emission from the Cosmic Dawn. These observations will complement indirect probes of the Dark Ages and Epoch of Reionization such as quasar sightlines, deep galaxy surveys, and the CMB optical depth which leave the reionization history of the universe only loosely constrained. (See Furlanetto et al. (2006); Morales & Wyithe (2010); Pritchard & Loeb (2012); Loeb & Furlanetto (2013); Zaroubi (2013) for reviews) Sensitivity and foreground removal are the main challenges in 21 cm observations, as the expected cosmological signal is 4–5 orders of magnitude fainter than Galactic and extragalactic foregrounds. Radio interferometers such as the Murchison Widefield Array (MWA) (Tingay et al. 2013; Bowman et al. 2013), the Precision Array for Probing the Epoch of Reionization (PAPER) (Ali et al. 2015b), the Giant Meterwave Radio Telescope (GMRT) (Paciga et al. 2011), and the Low Frequency Array (LOFAR) (van Haarlem et al. 2013) are seeking a first detection of cosmological 21 cm emission in power spectrum measurements, where the smooth frequency evolution of the foreground emission separates from the spectrally unsmooth cosmological signal whose frequency dimension probes the a line of sight through the inhomogenous reionizing universe.

The Hydrogen Epoch of Reionization Array (HERA) (Pober et al. 2014, , deBoer et al., submitted) is drawing on lessons learned by the MWA and PAPER to reach the calibration and foreground isolation accuracy required to make a significant detection and characterization of the cosmological signal. HERA uses 14 m diameter parabolic

dishes arranged in a compact, hexagonal array to achieve coherent integration on the very low surface brightness 21 cm signal. Redundant baselines also permit redundant calibration techniques which solve for internal degrees of freedom with only of parameters which must be estimated from the sky (Zheng et al. 2014), circumventing the sky model based calibration schemes which non-redundant arrays must pursue. HERA is pursuing a staged deployment of 19, 127, and finally 331 elements in progressively larger hex patterns, with scattered outriggers for imaging. A central lesson of first generation instruments is it is essential to characterize the instrument response to foreground emission lest instrument frequency dependence smear foreground power into cosmological signal modes.

It was initially thought that the foreground emission would be confined to the lowest few line of sight Fourier modes (e.g., Morales et al. 2006), however it was later realized that the interferometer’s frequency-dependent point spread function smears foreground power into a “wedge” shaped region in $(k_{\perp}, k_{\parallel})$ Fourier space (Datta et al. 2010; Dillon et al. 2014; Pober et al. 2013; Morales et al. 2012; Vedantham et al. 2012; Thyagarajan et al. 2013; Trott et al. 2012; Liu et al. 2014a,b). This effect is straightforward to understand for a single baseline which measures the sky intensity weighted by the complex sky fringe $e^{i\vec{k} \cdot \vec{b}}$, where $\vec{k} = \vec{k}(\theta, \phi, f)$ is the wave vector of the incident radiation, \vec{b} is the baseline vector in meters, and f is the observation frequency. Thus sources at different positions relative to the baseline vector manifest different frequency structure despite their intrinsically smooth spectra, but are geometrically limited by

the baseline length to a maximum frequency dependence of $e^{2\pi ifb/c}$. This limits the foreground contamination to a wedge shaped region in Fourier space with $k_{\parallel} < ak_{\perp}$, where k_{\perp} and k_{\parallel} represent spatial modes perpendicular and parallel to the line of sight, and a is a constant depending on the observational frequency and cosmology. The complement of the wedge is known as the “EOR window”.

It is convenient to phrase this description in terms of the delay in radiation arrival at the baseline’s two antennas, τ , where $\tau_{\max} = b/c$. Sources at low delay have little frequency structure, while those near $\tau = \tau_{\max}$ acquire the maximum frequency structure given the baseline length.

The fact that sources acquire frequency dependence based on their position on the sky tells us already that the primary beam strongly affects the aggregate frequency dependence of the foregrounds. The high delay regions of the sky lie near the horizon while low delay regions lie closer to zenith and also perpendicular to the baseline vector. Thyagarajan et al. (2015a) simulate the foreground contamination seen with a dipole beam, a phased array, and an Airy dish, and find that the latter suffers the least foreground leakage into $k_{\parallel} > 0$ modes due to its narrow main lobe and minimal sidelobe levels. To be sure, all are subject to the same geometric limits on foreground frequency-dependence limiting foreground bounding foreground emission within the wedge, but the emission from high delay is better suppressed using the Airy dish leaving much of the wedge effectively empty.

So long as foreground emission is perfectly contained in the wedge it is irrelevant how much or little of it there is, but the finite bandwidth and imperfect bandpass calibration of real instruments smear power beyond the geometrical edge of the wedge into the EOR window. Sources at higher delay appear closest to the edge of the wedge, and thus are most at risk of leaking into the EOR window due to these effects. In fact, Thyagarajan et al. (2015a); Thyagarajan et al. (2015b) observe in simulations and then in data that while naively we might expect minimal emission at the very edge of the wedge because typical near-horizon beam responses are so small, two effects can cause a relative brightening of emission at those maximal delays, creating a characteristic “pitchfork” shape. This horizon brightening is caused by the large solid angle subtended by the near-horizon regions of the sky, as well as the apparent shortening of baselines when viewed nearly on axis at these elevations. This second effect makes intermediate length baselines of tens to hundreds of meters sensitive to the very bright diffuse emission would not see from near zenith. Together, these effects can overcome the decline in beam sensitivity near the horizon. All these considerations highlight the antenna beam as a critical design parameter for 21 cm observatories.

This is the first in a series of four papers detailing the HERA element. In this work we study angular response of the dish and its implications for power spectrum measurements. The three companion papers present reflectometry measurements (Patra et al., submitted) and simulations (Ewall-Wice et al., submitted) of the dish frequency response, as well as detailed foreground simulations for HERA (Thyagarajan et al., submitted). A general description to the design of the HERA experiment

from an engineering point of view is given by DeBoer et al. (submitted). In essence, we require a large collecting area for sensitivity and minimal sidelobes and horizon response without incurring the large cost per collecting area of very large dishes. A dish is preferred to a large phased array as it has fewer degrees of freedom and reduced potential of antenna-to-antenna variation (Neben et al. 2015b, submitted). These factors naturally lead to a 14 m diameter parabolic dish with a dipole feed suspended at prime focus. The 352 dishes are positioned in a compact, hexagonal array permitting redundant baseline calibration and coherent integration in \vec{k} space (Zheng et al. 2014; Ali et al. 2015b).

In this paper we first characterize the angular response of a prototype HERA dish at the National Radio Astronomy Observatory–Green Bank. We use the beam mapping system of Neben et al. (2015) to measure the 137 MHz beam pattern using the ORBCOMM satellite constellation. We obtain beam measurements out to zenith angles of $\sim 60^{\circ}$ where the beam response is -35 dB relative to zenith, and compare with different numerical models. We characterize the dish beam at various feed heights to map out the focus and study beam errors due to feed misalignment. We compute the collecting areas and implied EOR power spectrum sensitivities of our measured beams. After verifying our numerical models, we consider the science implications of these beam patterns by foreground delay spectra at different baseline lengths and observing conditions to study when the horizon brightening effect is strongest, and thus, when foreground are most at risk of leaking into the EOR window.

In detail, we discuss the electromagnetic design and modeling of the dish in Section 2. We present the experimental setup of the beam mapping experiments and discuss their systematics, then review the ORBCOMM beam measurement system, in Section 3. We present our power pattern measurements in Section 4, and study the science implications of these beam measurements for foreground power spectra in Section 5, then conclude with discussion in Section 6.

2. DISH DESIGN AND MODELING

2.1. Design of the HERA Dish

We review here the design of the HERA dish, and refer to DeBoer et al. (submitted) for details. The 14 m HERA dish design is a departure from the large N-small D approach used by 21 cm observatories like PAPER and the MWA. Both observatories are actively pursuing power spectrum analyses using several year data runs, but the sheer data volume makes characterization and removal of systematics, as well as repeated or complementary analyses, challenging. A larger element was chosen for HERA primarily to economize data volume.

The HERA element is a 14 m diameter parabolic dish ($f/D \approx 0.32$) with a dual-polarized dipole feed (Fig. 1) suspended at prime focus. The dish surface is formed by sheets of wire attached to PVC tubes attached to supports at the edge of the dish and to a hub at the base. The feed is suspended with cables attached to three telephone poles around the dish. For feed maintenance purposes, a door is engineered into the dish surface on one mesh panel. The feed stands 17 in off a mesh back

plane surrounded by a XX in deep cylinder. The nominal dish focus is at 4.5 m from the dish surface to the feed back plane, though numerical models suggest the focus is closer to 5.3 m. The feed is designed to make the beams for both polarizations more similar to each other, and also to taper the dipole beam towards the edge of the dish to mitigate dish-dish coupling.

Feed/dish optimization studies are ongoing and these parameters may change in the final HERA array, but in this work we use the feed with these dimensions and study the beam the feed suspended at different heights. We study the position of the dish focus, the shape of the main lobe, the magnitude of the dish sidelobes, the degree of beam symmetry, the actual dish/feed efficiency (i.e., collecting area), and the expected level of antenna-to-antenna variation.



FIG. 1.— Prototype HERA feed set up outside the dish for preliminary characterization. This feed revision consists of a dual-polarized sleeved dipole offset 17 in from a XX in diameter back plane, surrounded by a XX in deep cylindrical skirt.

One cost of using fewer large antenna elements is a smaller field of view, but this is a small effect for 21 cm power spectrum analyses as our leverage on k modes comes primarily from k_{\parallel} modes along the line of sight (in the frequency dimension). More significant is frequency structure introduced by time domain reflections between the suspended feed detailed by Ewall-Wice et al. (submitted) with simulations and Patra et al. (submitted) with zenith reflectometry measurements.

2.2. *Dish Modeling*

I EMAILED DAVE AND RICH TO ASK THEM TO WRITE A FEW SENTENCES ABOUT THE CST AND HFSS DISH MODELS

3. EXPERIMENTAL SETUP

3.1. *ORBCOMM Beam Mapping System Review*

We briefly review the beam mapping system detailed by Neben et al. (2015), then discuss application of system for HERA dish measurements. The system takes advantage of the 137 MHz communications satellites operated by ORBCOMM Inc. as bright point sources which, by virtue of their number (~ 30), short orbital periods (~ 90

minutes), and orbital precession cover $\sim 65\%$ of the visible sky in just a few days. The coverage from the Green Bank site is limited by the fact that the satellites' orbital inclinations are all less than 45° .

Unlike celestial source beam measurements, where the flux may be assumed constant over the timescale of the measurement, satellite fluxes can vary rapidly due to changing distance, orientation, and transmission power. To correct for this, we measure the satellite flux in each ground polarization (EW and NS) using a simple, well-modeled reference antenna. Comparison of this measured power with that observed in the Antenna-Under-Test (AUT) gives the AUT beam response in the direction of the satellite. An equivalent interpretation of the measurement is that the power ratio between the AUT and the reference antenna gives the relative beam response in the satellite direction, and multiplication by the reference antenna model yields the desired AUT response. As discussed in Neben et al. (2015), this procedure correctly measures the response of the AUT to unpolarized radiation despite the fact that satellite signals are generally polarized.

In detail, we measure the dual-polarization RMS power received by each antenna in 512 2 kHz channels across the 137–138 MHz band. Each band power is averaged over ~ 0.2 sec. There are 0–3 satellites above the horizon at any given time transmitting on different ~ 15 kHz wide sub-bands in 137–138 MHz. By observing at many different frequencies, we probe the beam response in all these directions simultaneously. We compute the satellite positions using the orbital elements published by Celestrak¹ and the orbital integrator predict². However, the satellite frequencies vary occasionally to avoid interference within the constellation. Zheng et al. (2014) use interferometric phases to identify and exclude times when multiple satellites are in view. As our data acquisition system makes only total power measurements, we instead use an ORBCOMM interface box (typically supplied to commercial users of the network) to sync with passing satellites and record their identifier and transmission frequency during each pass.

In this way, beam measurements are built up along satellite tracks over the course of several days of integration, yielding typically 200–300 satellite pass. Each pass is processed separately to identify and exclude times of low signal-to-background when the satellite is low in the sky or in the off state of a pulsing sequence. At those times, then satellite flux no longer dominates over that of the diffuse Galactic background, and a power measurement no longer probes the response in only the satellite direction. The beam measurements are then gridded in horizontal coordinates in HEALPix (Górski et al. 2005) with a resolution of 1.8° ($n_{\text{side}}=32$). As a last quality control step to reject errant beam measurements due to RFI, for instance, we keep only the central 90% of ~ 50 measured beam values in each HEALPix cell.

3.2. *HERA-Green Bank: A three-element prototype array*

A 3-element HERA engineering prototype is being constructed at the National Radio Astronomy Observatory—

¹ <http://www.celestrak.com/NORAD/elements/orbcomm.txt>

² <http://www.qsl.net/kd2bd/predict.html>

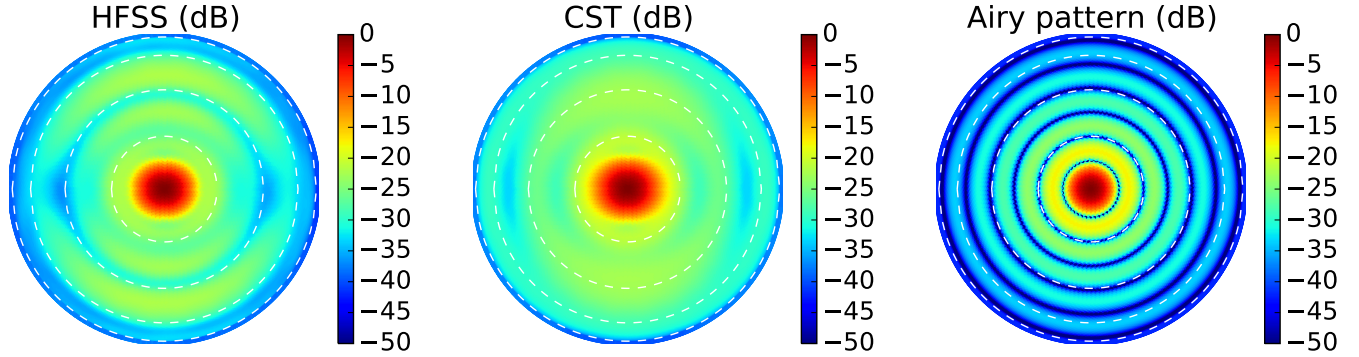


FIG. 2.— Simulated dish power patterns at 137 MHz (Sec. 2.2) using HFSS (left) and CST (middle) are shown beside an ideal Airy pattern for a 14 m diameter dish for comparison.

Green Bank. We performed the beam measurements presented in this work on the first of these dishes to be constructed, future work will characterize its beam in the presence of the other two dishes once they are constructed. The prototype array is situated in Galford Meadow, approximately 1 km southwest of the Green Bank Telescope. Note that unlike the full HERA site in the Karoo Desert Radio Astronomy Reserve in South Africa, the Green Bank site has trees and foothills, as well as moist ground. Our beam measurements are sensitive to these effects in addition to the construction imperfections of real world dishes.



FIG. 3.— The dish with its suspended feed is seen in the back, 50 m north of one of the reference antennas used in the null experiment to study systematics. The experiment is conducted in Galford Meadow at NRAO–Green Bank.

We use a simple dual-polarization dipole as our reference antenna. The dipole is constructed out of copper tubing covered by PVC for protection, mounted above a $2\text{ m} \times 2\text{ m}$ ground plane. See Neben et al. (2015) for details. During the dish measurements the dipole is positioned 100 m due south of the dish, though we experiment with other locations at first in our to characterize the environmental systematics of these measurements, as detailed in the next section. Figure 3 shows the dish with suspended feed 50 m north of one of the reference antennas.

3.3. Assessing Experimental Systematics

As in Neben et al. (2015), we assess systematics using a “null experiment” in which we use a second reference dipole as the antenna-under-test (AUT). Taking the ratio of its measured power pattern with the model beam pattern amounts to a ratio of the raw power responses received by the two antennas as a function of satellite direction. This probes the level of environmental systematics (i.e., reflections and varying ground properties) and antenna fabrication imperfections which affect each antenna differently. This is not a probe of modeling imperfections common to both antennas, but we expect such errors to be subdominant as the physical properties of the antenna are easier to characterize, and thus simulate, than misalignments and local environmental effects.

As we are not able to replace the HERA dish with a reference antenna, we run two null experiments with both reference dipoles deployed (1) 50 m apart on a NS line, 50 m south of the HERA dish; and (2) 100 m apart on a NS line, 100 m south of the HERA dish. Figure ?? shows the results from these experiments in the form of the ratio of the power responses of the two antennas. We collected roughly 100 satellite passes. Systematics at the few percent level are observed in within 20° of zenith, and at the 10 – 20% level farther out. The magnitude and angular distribution of these systematics changes modestly as the separation is changed, suggesting that the reference dipoles differ largely due to intrinsic differences, with some environmental variation. In any case, these fractional errors propagate directly into our measured dish power patterns.

4. DISH MEASUREMENTS

4.1. Power pattern measurements

We make three dish power pattern measurements with the feed at different heights: (1) 4.5 m, the nominal dish focus; (2) 5.0 m, an intermediate focus; and (3) 5.3 m, the numerically determined focus of the dish/feed system, where all heights are measured from the dish surface to the feed back plane. In each configuration we collect data for 2–4 days, obtaining roughly 200 satellite passes. We exclude times when the received power is within 20 dB of the background level determined at between passes, and then grid measured beam values into 1.8° HEALPix cells on the sky, rejecting outliers in the top or bottom 5% in each cell as a final guard against rare satellite identification problems or ADC saturation issues.

Figure 5 shows the measured power patterns for these three feed heights for the EW (left panel) and the NS

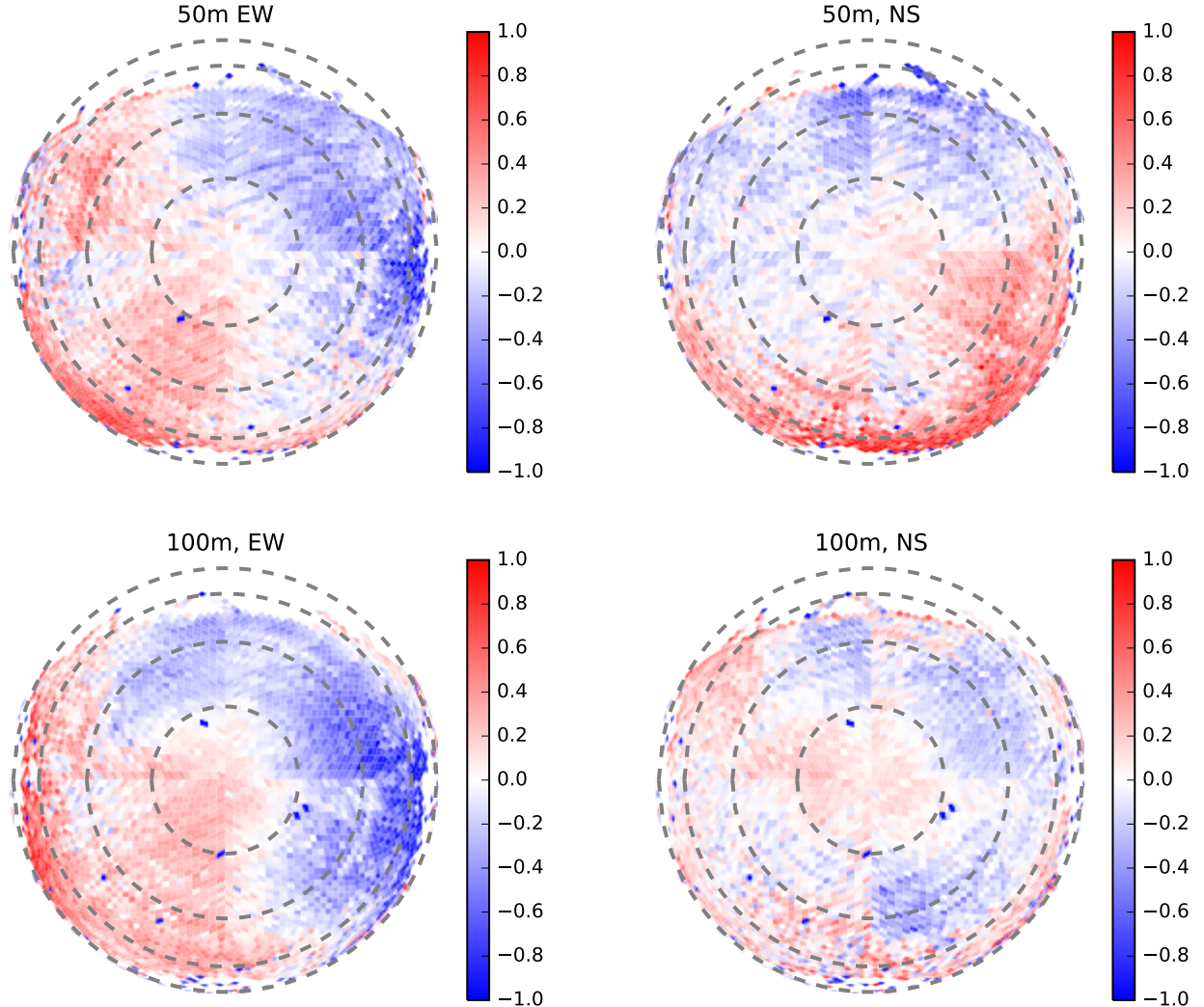


FIG. 4.— We characterize the accuracy of the beam measurement system through null experiments in which a second reference antenna is taken as the AUT and ratio of both reference antenna power patterns is measured for EW (left) and NS (right) polarizations. The reference antennas are separated by 50 m from each other and from the HERA dish in the first experiment (top), and by 100 m from each other and from the HERA dish in the second experiment (bottom).

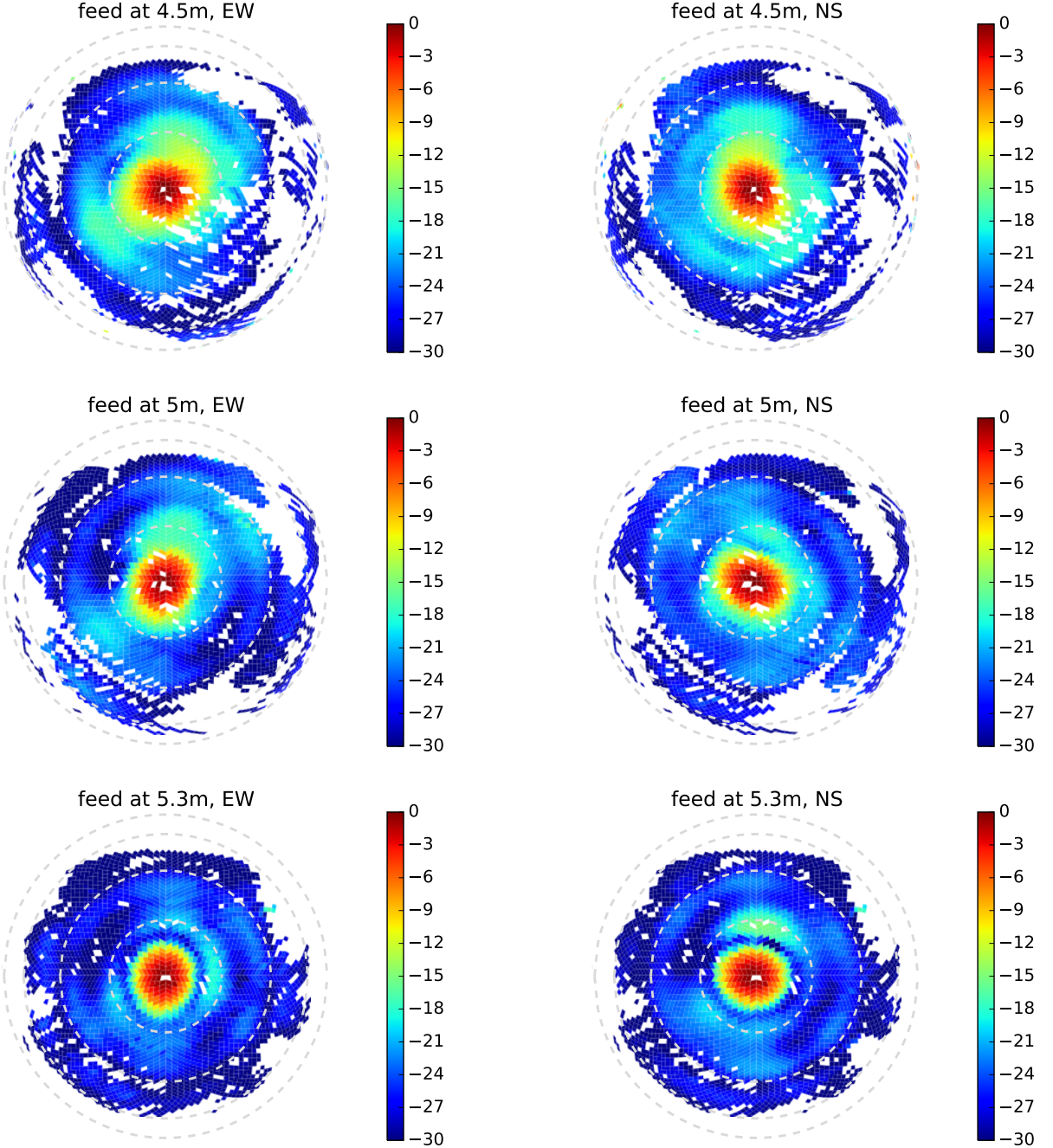


FIG. 5.— Measured dish power patterns at various feed heights for the EW (left panel) and NS (right panel) instrumental polarizations. The sidelobes shrink and the main lobe narrows as the feed is raised, confirming that the focus of the dish/feed system is higher than the 4.5 m ideal focus of the parabolic dish.

(right panel) feed polarization. These maps are plotted in sine-projection with dashed circles marking zenith angles of 20° , 40° , 60° , 80° . The sky coverage in these dish measurements extends out to typically $\theta \sim 50 - 60^\circ$. Beyond that the ORBCOMM flux is sufficiently attenuated relative to diffuse galactic emission that a power ratio measurement between the two antennas is no longer a clean probe of their gains in the direction of the satellite. At these zenith angles, the beam sidelobes are roughly -30 dB, and are trending downward at the edge of the measured region.

The roughly 10° main lobe narrows slightly as the feed

is raised from 4.5 m to 5.3 m, and the sidelobes shrink both in size and in amplitude, confirming the numerically predicted focus of 5.3 m. As expected, the EW main lobes are slightly wider in the NS direction. In theory, the only asymmetric part of the dish is the dipole feed, so the overall beam should have a 180° azimuthal symmetry. We observe deviations from this symmetry at the few dB level in the sidelobes, suggesting dish surface and/or feed imperfections given that the systematics identified in the null experiment are smaller.

Figure 6 shows slices through the E and H planes of these power patterns along with the HFSS and CST

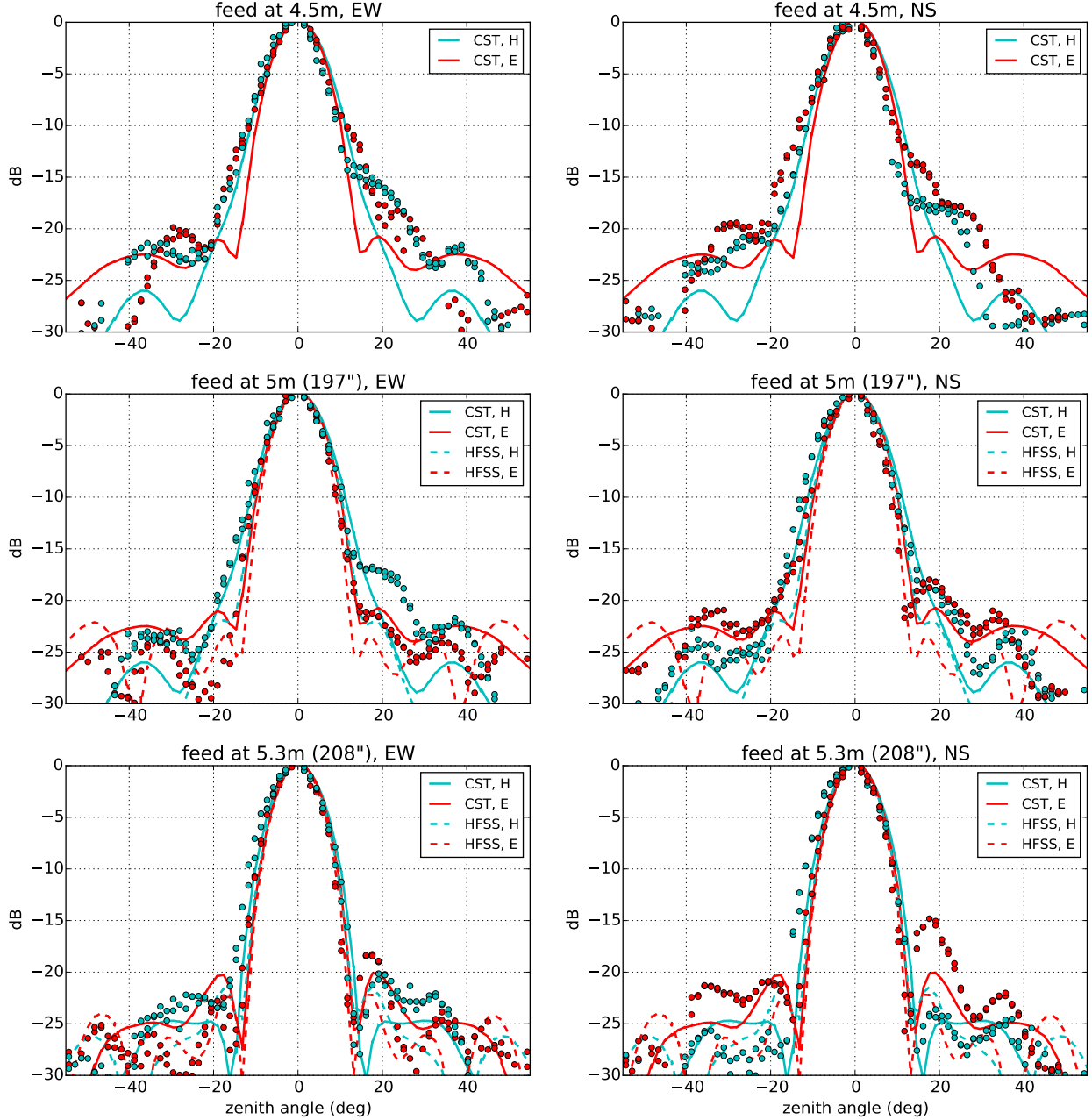


FIG. 6.— Slices through the E and H planes through the measured dish power patterns (points) and numerical models (curves). The measured beams agree with both models in the main lobe out to zenith angles of 15–20°, but begin to deviate in the sidelobes at the 0.1–0.5% level of the beam.

numerical models discussed earlier. As in the previous plot, the EW and NS beams are shown in the left and right panels, while the different feed heights are shown in the different rows. The data agree with both models to within a dB in the main lobe, but begin to diverge in the sidelobes at zenith angles of 20° and larger. Here the evolution of the sidelobes as the feed is raised is again seen starkly, as is the fact that the main lobes are slightly wider along the H planes than along the E planes.

4.2. Sensitivity

We compute the effective collecting areas of these beam patterns by first interpolating over unmeasured cells and smoothly extrapolating the power pattern to the horizon.

These operations produce a realistically smooth beam which reaches roughly -30 dB at the horizon, as suggested by the numerical models. The collecting area is related to the power pattern as

$$A = \frac{\lambda^2 B(0,0)}{\int B(\theta, \phi) d\Omega} \quad (1)$$

The collecting areas range are shown in Table 1 along with the maximal collecting area achieved by the Airy pattern for a 14 m dish. The measured collecting areas are a 30–50% lower than the geometric area. This is in line with expectations given that the Airy pattern has the largest possible collecting area, equal to the dish cross section, and the feed’s backplane and cylindrical skirt re-

duce it. However we opt for this reduction over added collecting area in order to reduces the azimuthal beam asymmetry and minimize the cross-coupling between adjacent dishes.

TABLE 1
COLLECTING AREA (m^2) OF MEASURED 137 MHz BEAMS AND CORRESPONDING POWER SPECTRUM SNR FOR HERA-127.

Beam	A_{eff} (m^2)	SNR (pess, mod, opt)
Airy pattern	155	9.1, 11.0, 37.2
Measured, feed at 5.3 m	97.9	8.2, 8.3, 29.2
Measured, feed at 5 m	82.6	6.8, 6.9, 26.5
Measured, feed at 4.5 m	73.6	6.4, 6.5, 24.8

We run 21cmSense³ to compute the overall SNR of a power spectrum detection with one season (6 hours per night for 180 nights) of HERA-127 data. To input these collecting areas into 21cmSense, we convert these measured dish collecting areas into effective dish diameters, which we input as the `dish_size_in_lambda` parameter. We predict the SNRs with optimistic, moderate, and pessimistic foreground assumptions. In the optimistic case, k modes inside the same uv pixel are added coherently, and all modes whose frequency dependence is larger than that of source at the edge of the main lobe are used. In the moderate case, k modes inside the same uv pixel are added coherently and only modes whose frequency dependence falls outside of the horizon plus a buffer are used. In the pessimistic case, all baselines are added incoherently and only modes outside the horizon plus a buffer are used.

The SNRs computed with the measured collecting areas fall from 9–11 for the Airy pattern to 6–8 in the pessimistic and moderate cases. In the optimistic case, the SNR falls from 37 with the Airy pattern to 24–29 with the measured collecting areas. In all cases this reduction is a loss of sensitivity, but a power spectrum detection is still always very significant at the 6σ level or better.

5. FOREGROUND DELAY SPECTRUM SIMULATIONS

We turn in this section to the effects of the beam power pattern on the apparent frequency dependence of the foregrounds. Thyagarajan et al., (submitted) discuss the apparent frequency dependence of foregrounds in more detail as well as methods to mitigate to mitigate it such as delay space CLEANing. We focus on this section on the uncertainties in these foreground power spectrum simulations due to beam modeling uncertainties, but we must first discuss these foreground simulations themselves and their dependence on observing conditions.

We simulate foreground power spectra using different primary beam models at various local sidereal times (LSTs). Given that our measured dish power patterns agree well with both numerical models (HFSS and CST) in the main lobe but deviate in the sidelobes, and that these models make somewhat different assumptions about the dish surface, we take them as a representative pair of possible dish models. We use a feed height of 5 m, a compromise between larger collecting area and smaller risk of coupling to adjacent dishes. We also include

the Airy pattern for comparison as Thyagarajan et al. (2015a). Beam models with weaker response near the horizon (such as the Airy pattern) downweight sources in this direction of high apparent frequency dependence. This reduces the magnitude of emission near the edge of the EOR window, reducing the risk it leaks inside. We use the per-baseline approach of Parsons et al. (2012b,a), simulating visibilities measured by specific baselines as a function of frequency, then computing the Fourier transform over frequency (delay transform) and normalizing the result into a cosmological power spectrum following Thyagarajan et al. (2015a).

In detail, we simulate visibilities for each beam model at various LSTs, modeling the sky as the sum of the Global Sky Model (de Oliveira-Costa et al. 2008) and the Culgoora (Slee 1995) and MWA Commissioning Survey (Hurley-Walker et al. 2014) point source catalogs. We use a frequency spacing of 1 MHz, sufficient to characterize delays within and just outside of the horizon limits on both baseline lengths we are concerned with, 14 m and 42 m. We use a total bandwidth of 100 MHz (50 MHz after applying the Blackman-Harris window) centered on 150 MHz. This bandwidth is larger than the 10 MHz thought to be safe from signal evolution over redshift, but is the bandwidth used in the wide band delay space foreground CLEAN of Parsons et al. (2014); Ali et al. (2015a).

Figure 7 (top panel) shows simulated foreground delay spectra at various LSTs using the nominal HFSS beam. As all these LSTs are high galactic latitudes far from the galactic center, the total visibility power (the level of the zero delay mode) varies only by a factor of a few over these LSTs on both baseline lengths (14 m (left panel), 42 m (right panel)). However the negative delay horizon limit (corresponding to the western horizon) has a peak that varies by over three orders of magnitude on the 14 m baseline and by two orders of magnitude on the 42 m baseline, demonstrating the stark difference in horizon brightening when the galaxy is just above versus just below the horizon.

In this figure we perform the approximate conversion from delay τ to k_{\parallel} , which we plot as a second x -axis at the top of the plot. For these short baselines, k_{\parallel} may be converted to k by adding $k_{\perp} = 0.005$ for the 14 m baseline or $k_{\perp} = 0.02$ for the 42 m baseline in quadrature. These numbers are small compared to the range of k_{\parallel} plotted, and thus we interpret the k_{\parallel} axis as simply the k axis, and plot a 1D model power spectrum computed using 21cmFast (Mesinger et al. 2011) as a dotted line for comparison.

To characterize the effect of beam modeling uncertainties on this horizon brightening, we select two of these LSTs, one with maximal horizon brightening (2°), and one with minimal horizon brightening (62°). Figure 8 shows the sine-projected Global Sky Model, which dominates the horizon brightening effect, in horizontal coordinates with units of Kelvin for both LSTs. Dashed lines mark zenith angles $20^\circ, 40^\circ, 60^\circ, 80^\circ$. These plots confirm that the large negative delay peak at the 2° LST is due to the center of the galaxy just above the horizon. In contrast several hours later, the galactic center is fully below the western horizon, leaving only a slight brightening near the eastern horizon due to the weaker galactic

³ <https://github.com/jpober/21cmSense>

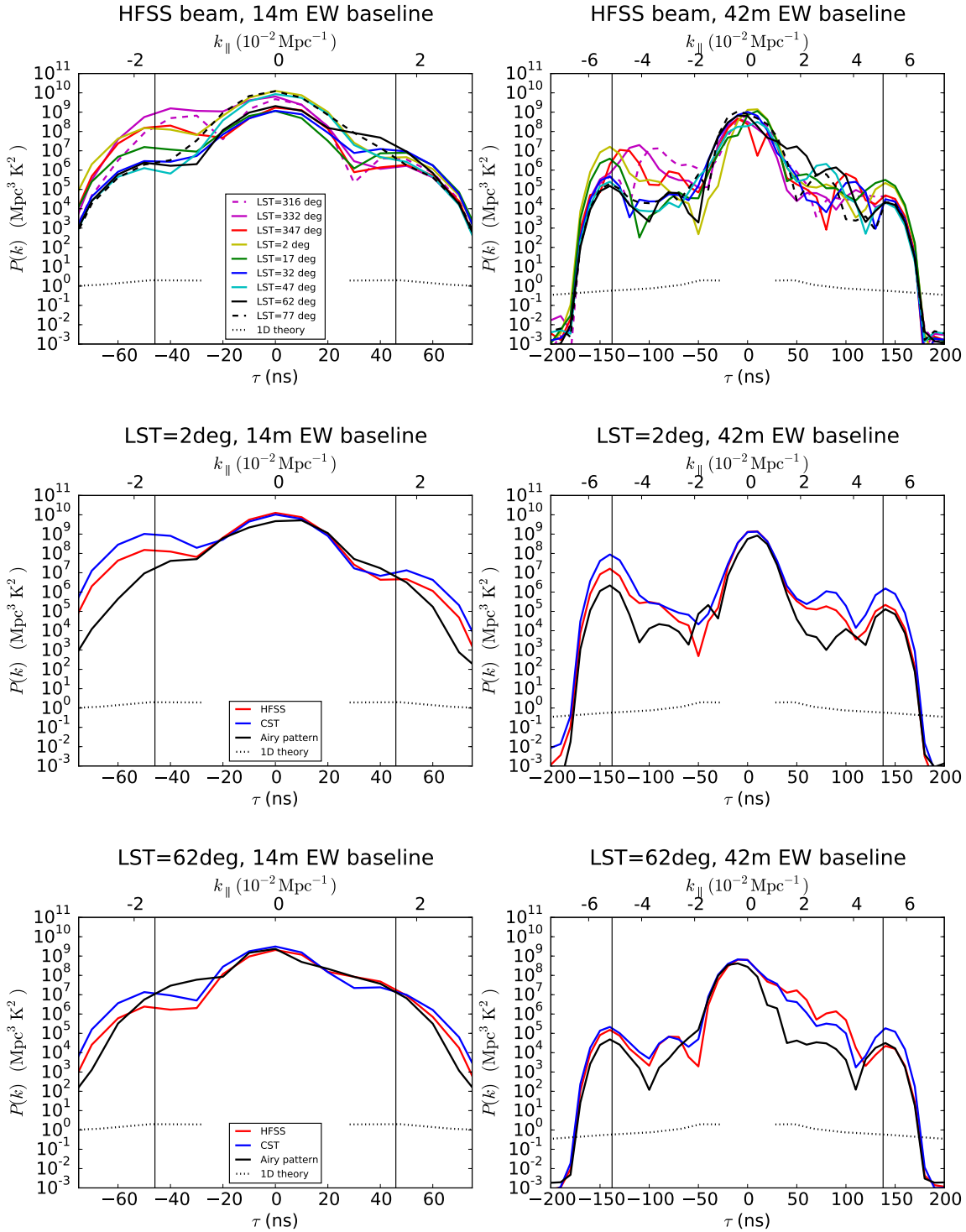


FIG. 7.— Simulated foreground delay spectra using the HFSS beam at various LSTs (top panel). We plot the delay spectra at two LSTs spanning the range of possible horizon brightening for three different beam models. The maximum horizon brightening at the negative horizon occurs at 2° LST (middle panel), and the three beam models thus differ markedly in their predicted delay spectra near the horizon. In contrast, when the horizon brightening effect is smaller at 2° LST, the foreground delay spectra from all three beams agree much more closely.

anticenter.

How much do the predicted foreground power spectra differ between the three model dish power patterns? Figure 7 (middle panel) shows the simulated delay spectra for all three beams at 2° LST, when the horizon brightening is worst. All three delay spectra agree out to delays of 10–20 ns on the 14 m baseline and 30–40 ns on the 40 m baseline. These numbers suggest that the beams track each other fairly well out to 15–20° from zenith, beyond which they diverge. This is roughly what is observed in Figure 6 (middle panel). At larger delays, especially near the negative delay horizon limit, all three model delay spectra diverge due to the significant edge brightening which effectively discriminates between these models. The CST, HFSS, and Airy beams reach roughly -35 dB, -38 dB, and -50 dB at the horizon (Figure 2), consistent with the fact that the CST beam has the largest horizon brightening, followed by the HFSS beam, and then by the Airy beam. This is seen in the delay spectra for both baseline lengths, though the edge brightening is much clearer on the longer baseline where it less diluted by zero delay emission.

In contrast, all three model agree much more closely when there is little or no edge brightening as in Figure 6 (bottom panel) where we plot the delay spectra for all three beams for 62° LST. There is still a modest flattening off near the horizon on the 14 m baseline and a slight peak on the 42 m baseline due to the large solid angle near the horizon. However as the near horizon emission at this LST is roughly the same temperature as emission from everywhere else on the sky, the difference between the three beam models is greatly reduced.

6. DISCUSSION

Power spectrum analyses by first generation 21 cm observatories are ongoing, but are contending with challenges ranging from calibration and foreground modeling to the analysis effort required to process thousands of hours of data. HERA draws on the most successful ideas from these first generation instruments, pursuing a compact and redundant array layout and collecting area antenna elements to minimize analysis cost. The hexagonal grid allows redundant calibration and coherent power spectrum integration, and the large 14 m dish achieves sufficient sensitivity at a reasonably data processing and analysis cost. The papers in this series characterize the 14 m diameter dish used as HERA’s antenna element using reflectometry measurements and simulations which probe its frequency response, as well as power pattern measurement which probe its angular response.

We present in this paper beam pattern measurements at 137 MHz and discuss their implications for 21 cm power spectrum analysis in terms of sensitivity and foreground isolation. We begin with the power pattern measurements using the beam mapping system of Neben et al. (2015) which we deploy at the prototype three-element HERA array at the National Radio Astronomy Observatory–Green Bank. Only one dish had been constructed when these measurements were made. We present measured power patterns for three dish configurations with the feed at different heights over the dish surface in order to characterize the focus of the system. The measured power patterns probe nearly two thirds of the visible sky, down to -30 dB relative to the zenith re-

sponse. The measured beams agree well with both models in the main lobe out to 10–20° from zenith, then roughly track the typical sidelobe levels at 20–30 dB below zenith though fail to reproduce the exact sidelobe amplitudes and locations.

These deviations away from models and away from 180° azimuthal symmetry are larger than the ±1 dB systematics observed in the null experiments which probe our beam measurement accuracy, suggesting they are genuine measurements of the in situ dish beam. The most likely dish non-idealities are dish surface imperfections and feed misalignment, both of which may vary from antenna to antenna in the full HERA array. Characterizing this antenna-to-antenna beam variation and its effects on power spectrum analyses for HERA, as Neben et al. (submitted) do for the MWA, is left as future work.

We quantify HERA’s 21 cm power spectrum sensitivity given our beam measurements by first computing the collecting area of the different dish configurations. We observe a reduction of 30–50% from the geometric cross section of a 14 m dish due to the dipole feed and its cylindrical skirt which tapers the beam towards the edge of the dish to mitigate cross coupling with adjacent dishes. We convert these collecting areas into effective dish sizes, then use 21cmSense to predict the overall power spectrum SNR with one season of HERA-127 data. We find SNRs of 6–8 in pessimistic and moderate foreground scenarios, and 24–29 in optimistic ones, to be compared with SNRs of roughly 10 and 37 using full geometric collecting area. While certainly a reduction from the theoretical limit, these sensitivities still permit a very significant detection of the 21 cm signal after a single observing season.

Beyond simple sensitivity considerations, though, the beam pattern affects science analyses by reweighting celestial emission in different regions of the sky, which are then imprinted with different frequency dependence by the interferometer. Longer baselines are proportionately more susceptible to this effect, giving rise to a “wedge” shaped region in 2D Fourier space. Thyagarajan et al. (2015a) has highlighted that the distribution of foregrounds *within* the wedge is important as well. If the beam response is sufficiently shallow at low elevations, there is a brightening of emission from near the horizon in line with the baseline due in part to the large solid angle at low elevations. This produces a characteristic “pitchfork” shape in the delay spectrum of a single baseline, with a zero delay peak due to bright near-zenith emission surrounded by tines at the negative and positive horizon limits due to emission from the two horizon directions in line with the baseline. These horizon peaks are *most* at risk of leaking foreground power into the EOR window given chromatic instrumental imperfections such as bandpass miscalibration.

We predict the magnitude of this effect for the HERA element as well as its dependence on beam modeling uncertainties. As expected, we find that the level of horizon brightening is largest when the galaxy is just above the horizon, and lowest when it is well below. When the pitchfork effect is large, its uncertainty is also large as seen in the deviation of the delay spectra with HFSS and CST beam models in these simulations. When the effect is small, the two beam models produce much more similar results, highlighting the delay spectrum as an exquisite

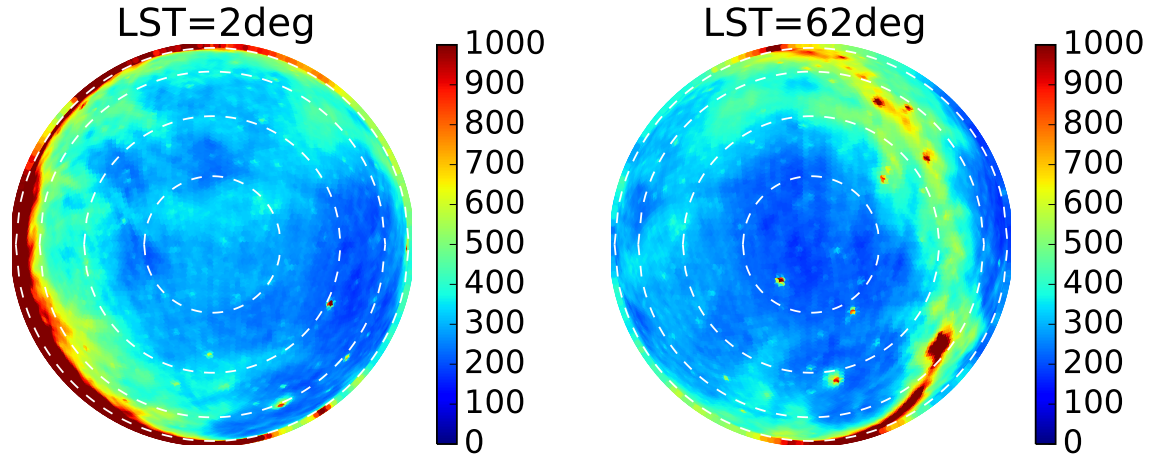


FIG. 8.— Global Sky Model (de Oliveira-Costa et al. 2008) in sine-projected horizontal coordinates at LST of 2° (left) and 62° right. The very bright emission from the center of the galaxy at the western horizon at 2° is seen in the delay spectra of EW baselines as a horizon brightening at negative delay.

probe of the challenging to measure beam response at very low elevations.

As discussed by the other papers in this series, the frequency dependence of the beam power pattern and its overall gain widen the delay kernel of a source, leaking power into the EOR window. These papers demonstrate that in the best case, a combination of bandpass calibration and delay space CLEANing can mitigate fore-

grounds to a manageable level, while in the worst case, HERA can still achieve a XX–XX σ detection of the EOR parameters from the power spectrum by simply excluding a very conservative buffer outside the wedge. All these considerations highlight the need for precision characterization of antenna elements and their implications for 21 cm science analyses on the part of next generation observatories if we are to have any hope of detecting making this challenging measurement.

REFERENCES

- Ali, Z. S., et al. 2015a, ApJ, 809, 61
 —. 2015b, ArXiv e-prints
 Bowman, J. D., et al. 2013, TrottObservingModes, 30
 Datta, A., Bowman, J. D., & Carilli, C. L. 2010, ApJ, 724, 526
 de Oliveira-Costa, A., Tegmark, M., Gaensler, B. M., Jonas, J., Landecker, T. L., & Reich, P. 2008, MNRAS, 388, 247
 Dillon, J. S., et al. 2014, Phys. Rev. D, 89, 023002
 Furlanetto, S., Oh, S., & Briggs, F. 2006, Physics Reports, 433, 181
 Górski, K. M., Hivon, E., Banday, A. J., Wandelt, B. D., Hansen, F. K., Reinecke, M., & Bartelmann, M. 2005, The Astrophysical Journal, 622, 759
 Hurley-Walker, N., et al. 2014, PASA, 31, 45
 Liu, A., Parsons, A. R., & Trott, C. M. 2014a, Phys. Rev. D, 90, 023018
 —. 2014b, Phys. Rev. D, 90, 023019
 Loeb, A., & Furlanetto, S. R. 2013, The First Galaxies In The Universe (Princeton University Press, Princeton, NJ)
 Mesinger, A., Furlanetto, S., & Cen, R. 2011, MNRAS, 411, 955
 Morales, M. F., Bowman, J. D., & Hewitt, J. N. 2006, ApJ, 648, 767
 Morales, M. F., Hazelton, B., Sullivan, I., & Beardsley, A. 2012, ApJ, 752, 137
 Morales, M. F., & Wyithe, J. S. B. 2010, Annual Reviews of Astronomy and Astrophysics, 48, 127
 Neben, A. R., et al. 2015, Radio Science, 50, 614
 Paciga, G., et al. 2011, Monthly Notices of the Royal Astronomical Society, 413, 1174
 Parsons, A., Pober, J., McQuinn, M., Jacobs, D., & Aguirre, J. 2012a, ApJ, 753, 81
 Parsons, A. R., Pober, J. C., Aguirre, J. E., Carilli, C. L., Jacobs, D. C., & Moore, D. F. 2012b, ApJ, 756, 165
 Parsons, A. R., et al. 2014, ApJ, 788, 106
 Pober, J. C., et al. 2013, ArXiv e-prints
 Pober, J. C., et al. 2014, The Astrophysical Journal, 782, 66
 Pritchard, J. R., & Loeb, A. 2012, Reports on Progress in Physics, 75, 086901
 Slee, O. B. 1995, Australian Journal of Physics, 48, 143
 Thyagarajan, N., et al. 2013, The Astrophysical Journal, 776, 6
 —. 2015a, ApJ, 804, 14
 Thyagarajan, N., et al. 2015b, ApJ, 807, L28
 Tingay, S. J., et al. 2013, Publications of the Astronomical Society of Australia, 30
 Trott, C. M., Wayth, R. B., & Tingay, S. J. 2012, ApJ, 757, 101
 van Haarlem, M. P., et al. 2013, A&A, 556, A2
 Vedantham, H., Udaya Shankar, N., & Subrahmanyan, R. 2012, ApJ, 745, 176
 Zaroubi, S. 2013, in Astrophysics and Space Science Library, Vol. 396, The First Galaxies, ed. T. Wiklind, B. Mobasher, & V. Bromm (Springer Berlin Heidelberg), 45–101
 Zheng, H., et al. 2014, Monthly Notices of the Royal Astronomical Society, 445, 1084
 Zheng, H., et al. 2014, MNRAS, 445, 1084